



Promising Antimicrobial and Azo Dye Removal Activities of Citric Acid-Functionalized Magnesium Ferrite Nanoparticles

Ahmed M. El-Khawaga¹ · Ayman A. Farrag^{2,3} · Mohamed A. Elsayed¹ · Gharieb S. El-Sayyad^{1,4} · Ahmed I. El-Batal⁴

Received: 7 May 2020 / Accepted: 13 November 2020 / Published online: 2 January 2021
© Springer Science+Business Media, LLC, part of Springer Nature 2021

Abstract

In this study magnesium ferrite nanoparticles (MgFe_2O_4 NPs) were synthesized through an aqueous co-precipitation method and functionalized with citric acid (CA) for outstanding their antimicrobial potential and removal activity of azo dye. MgFe_2O_4 NPs and CA- MgFe_2O_4 NPs were characterized by XRD, HRTEM, SEM, EDX, FT-IR, and SEM/EDX mapping method to analyze crystallinity, average particle size, morphology, functional groups and elemental composition, respectively. Antimicrobial activity was investigated against pathogenic bacteria and yeast as zone of inhibition (ZOI) and minimum inhibitory concentration (MIC). Reaction mechanism using SEM/EDX analysis of CA- MgFe_2O_4 NPs-treated microbial cells was mentioned. The removal efficiency was tested against methyl orange (MO), and various parameters affecting the removal efficiency such as (pH on removal of MO, MO initial concentration, and CA- MgFe_2O_4 dose) were studied. Antimicrobial results showed that CA- MgFe_2O_4 NPs demonstrated maximum activities against *S. aureus*, *E. coli*, and *C. albicans* with ZOI of 20.0, 16.0, and 14.0 mm, respectively. Results obtained suggested that 0.1 g of CA- MgFe_2O_4 NPs achieved 85.0% removal of MO at pH 5.0.0, hence, it exhibited efficient dye removal and sufficient antimicrobial activities.

Keywords Surface modification · *Escherichia coli* · Methyl orange · SEM/EDX mapping technique · Reaction mechanism · Co-precipitation method

Introduction

Water contamination is one of the most serious factors affecting public health, terrestrial and aquatic environments [1]. The natural environment is under serious threat due to rapidly-expanding industrialization across the globe. Availability of pure water and sustainable water treatment technique is of great demand from industrial, societal, and environmental point of view. Due to the huge water pollution, increasing attention has been paid to water treatment in the past few decades [2, 3].

Wastewater from textile, leather tanning, food processing, paper making, plastic, ceramic and pharmaceutical industries are a major source of pollutant dye. Exposure of pollutant dyes in aqueous media is a serious concern to the recent environmental scientists due to their possible carcinogenicity, reproductive toxicity, neurotoxicity, and other skin- and eye-related problems [4]. Owing to their complex aromatic structure and synthetic origin, dyes are

✉ Ahmed M. El-Khawaga
ahmedelkhwaga15@gmail.com

✉ Gharieb S. El-Sayyad
Gharieb.Elsayyad@eaea.org.eg

¹ Chemical Engineering Department, Military Technical College (MTC), Egyptian Armed Forces, Cairo, Egypt

² Chairman of Botany and Microbiology Department, Faculty of Science (Boys), Al-Azhar University, Cairo, Egypt

³ Director of Al-Azhar Center for Fermentation Biotechnology and Applied Microbiology, Al-Azhar University, Cairo, Egypt

⁴ Drug Microbiology Lab, Drug Radiation Research Department, National Center for Radiation Research and Technology (NCRRT), Egyptian Atomic Energy Authority (EAEA), Cairo, Egypt

stable to light, oxidation, and biodegradable process, which provides them a long exposure time in the environment [5, 6]. Hence, removal of dyes from industrial effluents has become imperative not only to protect human health but also for the protection of the natural environment [7, 8].

Several conventional methods for water treatment are in investigation such as adsorption [9–11], chemical precipitation/oxidation [12, 13], ion-exchange [14], and photocatalytic discoloration [15–18], while among them, adsorption process becomes most favorable due to its simplicity, high efficiency, low operating cost, and less sludge production [19–21]. The economics and versatility of adsorption process are largely-dependent upon the adsorbent material and various low-cost adsorbents, such as hen feather, egg shell powder, bottom ash, and egg shell membrane [22–25], which have been reported in the literature for removal of dyes as well as heavy metals from wastewater.

One of the recent promising ways to improve the water treatment technology is based on nano-science [26], where the materials at the nano-scale appear with profound functionality [27]. Metal oxides have been studied extensively for improving their functionality and exploring their outstanding physical properties in low dimension [28–30]. Nano-materials possess relatively-higher degree of chemical, physical and biological activities due to their large surface area with respect to their bulk counterparts [31–35].

The most critical pathogenic bacteria producing a rapid resistance to the used antibiotics are *E. coli* and *S. aureus*, and they immediately-separated from the intestinal area of human and some animals. *E. coli* produces enteric disease, and different species create further intestinal dysfunction like urinary tract infection (UTI) [36]. Various NPs were tested for their antimicrobial activity by applying the agar-disc distribution method [37, 38]. They were recognized against various pathogenic bacteria and yeasts.

This study was performed with the following objectives: firstly to synthesize a highly-crystalline MgFe_2O_4 NPs by a very simple chemical co-precipitation method, surface modified by citric acid and to characterize its subsequent physical properties; secondly to explore the applicability for removal of a pollutant anionic dye of methyl orange (MO) from aqueous media. MO belongs to the azo dyes family and is known to be carcinogenic and mutagenic organic substance, which was widely-used in paper manufacturing, pharmaceutical, food industries, and also in research laboratories as an acid–base indicator [39, 40], and finally to determine the antimicrobial activities of MgFe_2O_4 NPs, and CA- MgFe_2O_4 NPs against some pathogenic bacteria and yeast.

Experimental Work

Materials

Ferric chloride hexahydrate ($\text{FeCl}_3 \cdot 6\text{H}_2\text{O}$), magnesium chloride hexahydrate ($\text{MgCl}_2 \cdot 6\text{H}_2\text{O}$) and citric acid were obtained from Merck, India. All the chemicals were used without further purification. Water used throughout the experiment was ultrapure milli-Q water. Methyl orange was obtained from s.d. fine-chem. pvt. (Limited, India).

Synthesis and Surface Modification of MgFe_2O_4 NPs

Magnesium ferrite nanoparticles (MgFe_2O_4 NPs) were prepared by co-precipitation method [41–43]. In this method 2.0 M of ferric chloride hexahydrate ($\text{FeCl}_3 \cdot 6\text{H}_2\text{O}$) and 1.0 M of magnesium chloride hexahydrate ($\text{MgCl}_2 \cdot 6\text{H}_2\text{O}$) were dissolved in 20 ml distilled water. The pH of the solution was maintained at 8 and stirred for 2.0 h. The neutralization was carried out with sodium hydroxide (NaOH) solution and the reaction temperature was maintained at 60 °C. The precipitate was thoroughly-washed with distilled water until it was freed from impurities. The product was dried at a temperature of 100 °C to remove the water contents. The dried powder was mixed homogeneously and sintered at 600 °C as represented in Scheme 1.

The surface of MgFe_2O_4 NPs was stabilized with citric acid by a direct addition method [44], to obtain modified MgFe_2O_4 NPs with carboxylic groups. Briefly, the MgFe_2O_4 NPs surface were treated with citrate ions by incubating for 1.0 h within 0.5 g/ml citric acid solution and reaction temperature was raised up to 90 °C and the reaction was completed for 60 min with continuous stirring.

The black precipitates were acquired by cooling the reaction mixture to room temperature. At last the suspensions were washed several times with de-ionized water. The particles did not settle down under the influence of magnet, as a result of stability of solution. The as-formed reaction product contained an excess of citric acid and so, the NPs dispersion was centrifuged and washed several times as exhibited in Scheme 1. MgFe_2O_4 NPs stabilized with citric acid were abbreviated as CA- MgFe_2O_4 NPs.

Characterization of MgFe_2O_4 NPs, and CA- MgFe_2O_4 NPs

The synthesized CA- MgFe_2O_4 NPs and MgFe_2O_4 NPs were characterized at central laboratories of National Center for Radiation Research and Technology (NCRRT), Egyptian Atomic Energy Authority (EAEA) and Military



Scheme 1 The systematic representation of the synthesis and surface modification of MgFe_2O_4 NPs by citric acid (CA)

Technical College, Egyptian Armed Forces using different techniques and instruments.

The functional groups composition and surface functionality of CA- MgFe_2O_4 NPs, MgFe_2O_4 NPs and CA were revealed by FT-IR spectra. FT-IR spectrum was a vital target that gives information regarding the chemical functional groups presented in citric acid. The experiments were carried out by a JASCO FT-IR 3600 Infra-Red spectrometer after applied KBr pellet technique. It was determined at a wave number range from 400 to 4000 cm^{-1} .

The crystallinity, phase analysis and the crystallite size and/or lattice of the synthesized MgFe_2O_4 NPs, and CA- MgFe_2O_4 NPs were determined by the XRD-6000, Shimadzu apparatus, SSI, Japan. The intensity of the diffracted X-rays was estimated as diffracted angle 2θ . Additionally, the average crystallite size was calculated by applying Williamson–Hall (W–H) method [45], according to the following equation (Eq. 1)

$$\beta \cos \theta = \frac{k\lambda}{D_{W-H}} + 4\varepsilon \sin \theta \quad (1)$$

where D_{W-H} is the average crystallite size, β is the full-width at half maximum, λ is the X-ray wavelength, θ is the Bragg's angle, k is a constant and ε is the strain of the samples.

The size and shape of the synthesized CA- MgFe_2O_4 NPs and MgFe_2O_4 NPs were evaluated by using High-Resolution Transmission Electron Microscope (HRTEM, JEM2100, Jeol, Japan). The surface morphology and grain size of the synthesized CA- MgFe_2O_4 NPs and MgFe_2O_4 NPs were investigated by SEM, ZEISS, EVO-MA10, Germany. Additionally, EDX (BRUKER, Nano GmbH, D-12489, 410-M, Germany) analysis was used to estimate the elemental structure, purity and the percentage of each metal in the structured CA- MgFe_2O_4 NPs, and MgFe_2O_4 NPs. The mapping analysis after applied SEM/EDX technique was used to attain a whole information about the clarity, distribution and the position of the metals in the

coated CA-MgFe₂O₄ NPs, and MgFe₂O₄ NPs. Finally, the indirect measurement of the surface charges of CA-MgFe₂O₄ NPs and MgFe₂O₄ NPs was estimated by the zeta potential analyzer (Malvern devise, UK) at different pH.

Dye Removal Method

The studies of the synthesized pure MgFe₂O₄ NPs and citrate functionalized respective MgFe₂O₄ NPs (CA-MgFe₂O₄ NPs) for removal of MO were performed with batch equilibrium method [46]. A stock solution (100 mg/l) of MO was prepared by dissolving 0.1 g of MO powder in de-ionized water, and experimental solutions of desired MO concentrations were obtained by successive dilutions of the stock solution with de-ionized water.

The batch experiments were carried out by taking 50 ml of MO solution of known concentration in a 125 ml flask. A total of 0.1 g CA-MgFe₂O₄ was added to each flask, and mixture was agitated at room temperature using a magnetic stirrer with constant speed of 250 rpm for a predetermined time to attain the equilibrium.

After removal equilibrium was achieved, the supernatant was separated from the CA-MgFe₂O₄ by magnet and the MO removal was monitored spectrophotometrically at the absorbance maximum of MO dye viz. $\lambda_{\max} = 464$ nm using Agilent Cary 60 UV-Vis spectrophotometer.

The pH of the aqueous solution was measured by a bench top pH meter (Hach, SensION), and pH of the solution was adjusted to desired values using dilute HCl/NaOH before the addition of CA-MgFe₂O₄ NPs.

The degree of decolorization (DD) of the sample was determined by using the relation (Eq. 2).

$$DD\% = (C_i - C_t)C_i \times 100 \quad (2)$$

where C_i is the initial absorbance of the sample and C_t is the absorbance at time t .

The MO removal study was performed by varying conditions like pH and temperature. The effect of initial dye concentration and effect of MO volume on dye removal was also investigated under similar experimental conditions. For accurate calculation of the amount removal, a calibration curve was obtained at $\lambda_{\max} = 464.0$ nm by the use of a series of standard solutions with different concentrations of MO.

Antimicrobial Activity Measurements of CA, CA-MgFe₂O₄ NPs and MgFe₂O₄ NPs

The synthesized CA-MgFe₂O₄ NPs, MgFe₂O₄ NPs (20.0 μ g/ml), and CA were tested for their antimicrobial potential through an agar-disc distribution method [47–51]. All samples were examined upon several resistant isolates of human urinary tract infection bacteria which received

from the culture collections in Drug Microbiology Lab., Drug Radiation Research Dep., NCRRT, Cairo, Egypt.

The pathogenic bacteria were separated from urine samples of UTI-patients. Bacterial strains were *Escherichia coli*, *Staphylococcus aureus*, *Bacillus subtilis*, *Pseudomonas aeruginosa* and *Candida albicans*. The bacterial inoculums were fixed at 0.5 McFarland (1–3) $\times 10^8$ CFU/ml, applying fixed 600 nm UV-Vis. spectrophotometer [52]. The growth restraint of all the investigated bacterial strains was estimated by the zone of inhibition (ZOI) after 24 h incubation [48, 53, 54]. Standard antibiotic discs such as Gentamycin (CN; 20 μ g/ml; 6.0 mm diameter), and Nystatin (NS; 100 μ g/ml), was chosen to determine the performance of the considered magnetic NPs.

The serial dilutions method of Luria–Bertani (LB) medium was applied to determine the minimum inhibitory concentrations (MIC) of the tested CA-MgFe₂O₄ NPs and MgFe₂O₄ NPs [49, 55]. For these determinations, a negative control such as the medium broth, positive control such as the examined pathogenic microbes and the used medium broth and CA-MgFe₂O₄ NPs and MgFe₂O₄ NPs (beginning with concentration = 20.0 μ g/ml) were applied. MIC was determined after 24 h of incubation at 36.0 ± 1.0 °C [56].

The inoculums were fixed as mentioned-before in the first antimicrobial screening [52]. MIC was defined by using the ELISA plate method after setting the fixed wavelength at 600 nm [56, 57]. The MIC was described as the lowest concentration of CA-MgFe₂O₄ NPs and MgFe₂O₄ NPs that inhibits 99.0% of the growth of the tested bacteria and yeast cells.

Reaction mechanism using SEM/EDX analysis of CA-MgFe₂O₄ NPs-treated microbial cells

Bacterial, and yeast cells from the antimicrobial test were washed with PBS and fixed with 3% glutaraldehyde solution. The preserved bacterial, and yeast specimens were regularly-washed with PBS and evenly-dehydrated with various concentrations of ethanol (30%, 50%, 70%, 80%, 95%, and 100%) for about 20 min at 28 ± 2 °C [58]. Next, bacterial, and yeast cells were placed on an aluminum scrap for SEM/EDX analysis [58]. The morphological characteristics of the control (non-treated pathogenic bacteria and yeast) and CA-MgFe₂O₄ NPs-treated bacterial and yeast cells were observed using SEM/EDX analysis.

Statistical Analysis

The mathematical analysis of the effects was conducted by applying the ONE WAY ANOVA (at $P < 0.05$), the least significant differences (LSD), and Duncan's multiple

systems [59]. The effects and data were examined and decided through SPSS software (version 15).

Results and Discussion

Synthesis of Functionalized MgFe_2O_4 NPs

Here the MgFe_2O_4 NPs were prepared by a chemical coprecipitation method with minor modifications of earlier reported methods [60, 61]. An inexpensive citric acid is used as a capping agent containing three carboxyl groups per molecule and undergoes easy formation of an organic monolayer on the surface of NPs. These mono-layers render the NPs stable with respect to aggregation and keep them well dispersed in aqueous media.

Functional Groups Identification of CA- MgFe_2O_4 NPs and MgFe_2O_4 NPs Using FT-IR Spectrum Analysis

To confirm the binding of citric acid on the surface of MgFe_2O_4 NPs, FT-IR studies were performed. The FT-IR spectra of pure MgFe_2O_4 NPs and citric acid modified MgFe_2O_4 NPs are displayed in Fig. 1.

The two intense peaks observed between 580 and 484 cm^{-1} were attributed to the stretching vibration mode associated to the metal–oxygen (Fe–O) bond in the crystalline lattice of Fe_2O_4 NPs. They are characteristically-pronounced for all spinel structures and for ferrites in particular [62, 63]. In overall, spinel ferrites exhibit two inherent vibrational bands, ν_1 and ν_2 and are corresponding to the stretching vibration of tetrahedral groups (A-site) and the stretching vibration of octahedral groups (B-site), respectively [64].

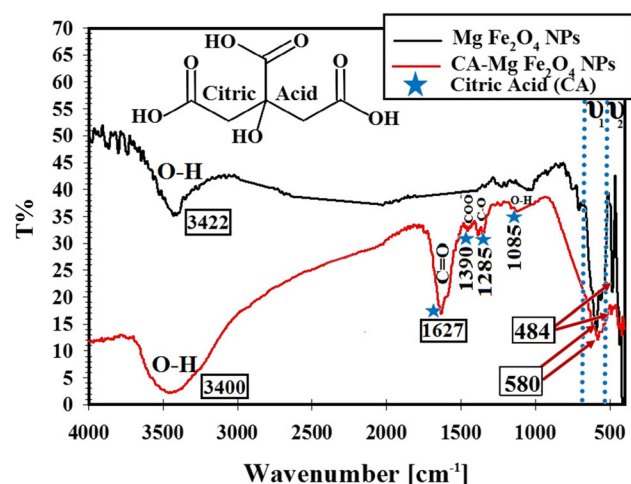


Fig. 1 FTIR spectra of pure MgFe_2O_4 NPs and citric acid modified MgFe_2O_4 NPs

A broad bands centered at 3400 and 3422 cm^{-1} were related to the presence of hydroxyl groups and attributed to OH-stretching. Since the NPs have been thoroughly-washed after synthesis, no mechanically-deposited citric acid is expected. New intense absorption peaks located at 1627 cm^{-1} , 1390 cm^{-1} and 1350 cm^{-1} as well as lower intensity peaks at 1285 cm^{-1} and 1085 cm^{-1} appears in the FT-IR spectra of CA- MgFe_2O_4 NPs. The 1730 cm^{-1} peak of a standard citric acid assignable to the stretching vibration of C = O from the COOH group [65, 66], shifts to the intense band at about 1627 cm^{-1} for CA- MgFe_2O_4 NPs. This reveals that carboxylate groups of citric acid should complex with the Fe atoms on the magnetite surface and render a partial single bond character to the C=O bond, weakening it, and shifting the stretching frequency to a lower value.

Furthermore, the vibrational modes appearing at 1390 cm^{-1} , 1285 cm^{-1} and 1085 cm^{-1} in CA- MgFe_2O_4 NPs were correspond to the symmetric stretching of COO^- , symmetric stretching of C–O, and OH group of citric acid. It has been proposed that citric acid binds to the magnetite surface by chemisorption of the carboxylate, that is, citrate ions [65].

Phase Analysis and the Crystallite Size Determination of CA- MgFe_2O_4 NPs and MgFe_2O_4 NPs Using XRD Spectroscopy

Figure 2 shows XRD pattern of CA- MgFe_2O_4 , and MgFe_2O_4 NPs nanopowder which treated and annealing up to 150 $^\circ\text{C}$ for 24 h. The diffraction peaks agree with the international standard diffraction data card, JCPDS number 89-4924, and provide a clear evidence of MgFe_2O_4 NPs formation, in both samples (Fig. 2a, b). This indicates the existence of a cubic spinel structure. The most intense reflections observed at 2θ values of 32.5 $^\circ$, 35.56 $^\circ$, 43.09 $^\circ$, 47.57 $^\circ$, 57.21 $^\circ$, 62.69 $^\circ$, and 74.57 $^\circ$ are assigned to (200), (311), (400), (422), (511), (440), and (533) planes of cubic spinel structure.

This lattice parameter is determined to be 8.366 Å, and the average crystal size was determined to be 16.45 nm and 18.35 nm for CA- MgFe_2O_4 NPs and MgFe_2O_4 NPs, respectively. The line broadening of the X-ray diffraction pattern gives a clear evidence for the nanometer range of the synthesized powder.

Additionally, as noted in Fig. 2b, additional diffraction peaks were recognized at 12.45 $^\circ$, 17.54 $^\circ$, 26.14 $^\circ$, and 31.25 $^\circ$ which corresponding to citric acid (CA) [67, 68], and confirmed the loading of CA along with the synthesized MgFe_2O_4 NPs.

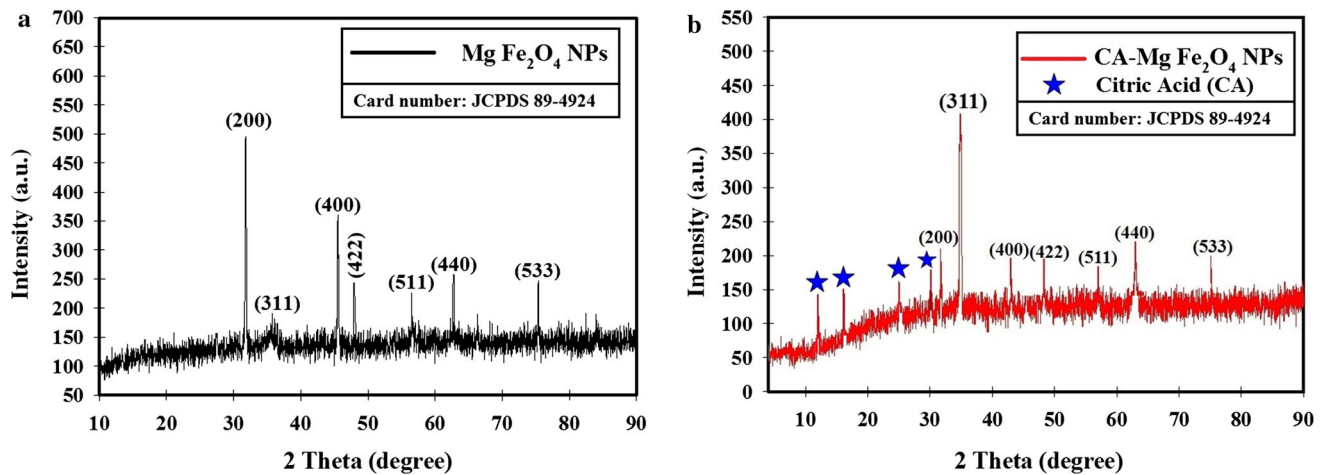


Fig. 2 XRD pattern of **a** MgFe_2O_4 NPs, and **b** $\text{CA-MgFe}_2\text{O}_4$ NPs

Surface Morphology of the Synthesized $\text{CA-MgFe}_2\text{O}_4$ NPs and MgFe_2O_4 NPs Using SEM Imaging Technique

SEM was used to prove the formation and the morphology of the synthesized $\text{CA-MgFe}_2\text{O}_4$ NPs and MgFe_2O_4 NPs [55, 69]. SEM images of the fabricated MgFe_2O_4 NPs are shown in Fig. 3a, and for $\text{CA-MgFe}_2\text{O}_4$ NPs in Fig. 3b.

For the synthesized MgFe_2O_4 NPs, the bright particles represented the Mg ferrites which appear normally-distributed as shown in Fig. 3a. Also for $\text{CA-MgFe}_2\text{O}_4$ NPs, MgFe_2O_4 NPs were located at the core, while the CA was coated this core, producing CA-functionalized MgFe_2O_4 NPs. The surface behavior reveals inhomogeneous grain appearance with remarkable smooth agglomerates can be observed due to the occupation of a large quantity of Mg at the grain boundary which could control the grain growth [70].

Also, the surface is remarkably-porous and presents a coalescing the form of the agglomerated particles connected with the interfacial surface tension phenomena. The appearance of the microstructural characteristics can be associated with the matter transport mechanism between the near grains during the sintering process.

Elemental Analysis and Purity Determination of the Synthesized $\text{CA-MgFe}_2\text{O}_4$ NPs and MgFe_2O_4 NPs Using EDX Spectral Analysis

EDX quantitatively-uses to investigate the elemental composition of $\text{CA-MgFe}_2\text{O}_4$ NPs, and MgFe_2O_4 NPs [71]. Figure 4a represented EDX analysis of the synthesized MgFe_2O_4 NPs which confirms the purity of the synthesized Mg ferrites as the detected elements are C, O, Mg and Fe atoms and the presented C atom was attributed to the carbon holder which used for the imaging process.

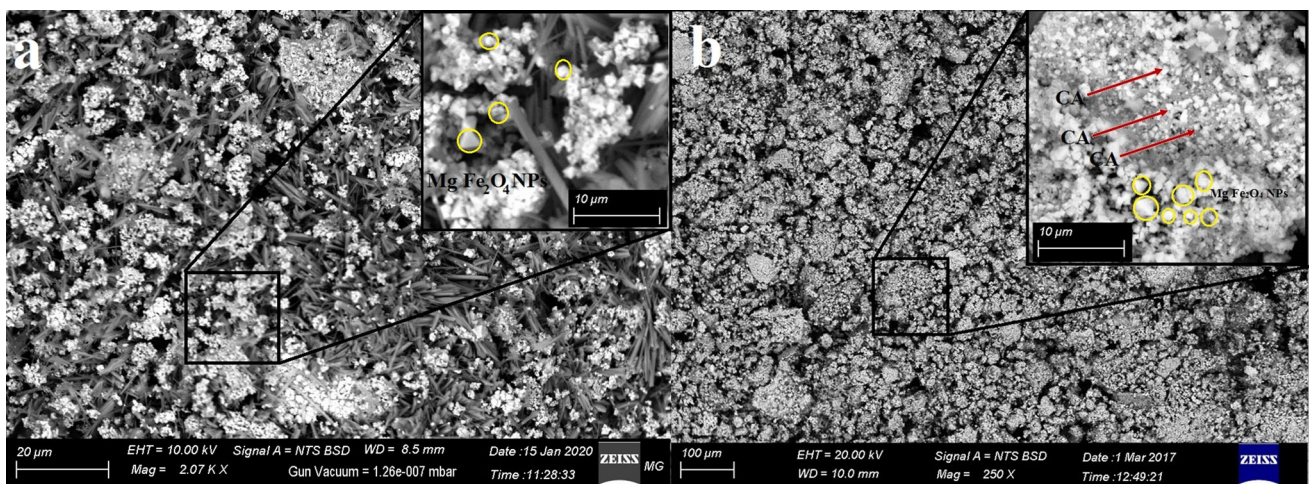


Fig. 3 Surface morphology investigation of **a** MgFe_2O_4 NPs, and **b** $\text{CA-MgFe}_2\text{O}_4$ NPs using SEM imaging method

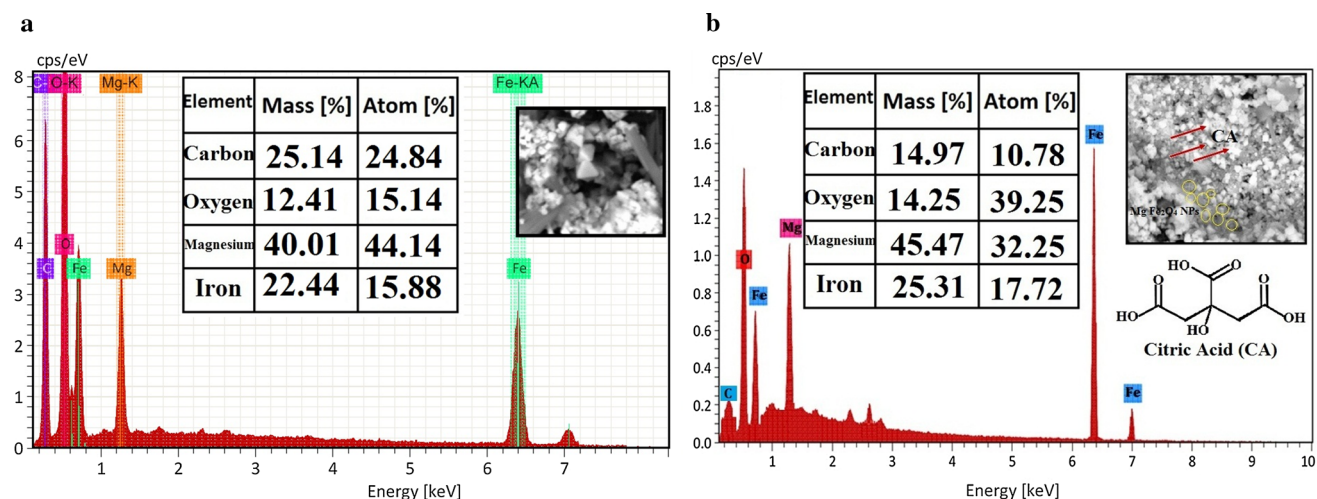


Fig. 4 Elemental analysis of **a** MgFe_2O_4 NPs, and **b** $\text{CA-MgFe}_2\text{O}_4$ NPs using EDX spectroscopic analysis

Figure 4b shows EDX analysis of the synthesized $\text{CA-MgFe}_2\text{O}_4$ NPs revealing its particle dispersion with high purity by the appearance of C, O, Mg and Fe atoms. The recorded carbon and oxygen atoms attributes to citric acid loaded on the surface of MgFe_2O_4 NPs. The corresponding EDX elemental analysis confirmed the presence of all constituent atoms producing the $\text{CA-MgFe}_2\text{O}_4$ NPs.

Chemical Mapping of the Synthesized $\text{CA-MgFe}_2\text{O}_4$ NPs and MgFe_2O_4 NPs Using SEM/EDX Coupled Spectral Analysis

The elemental mapping images of the integrated $\text{CA-MgFe}_2\text{O}_4$ NPs and MgFe_2O_4 NPs were showed in Fig. 5. For the synthesized MgFe_2O_4 NPs (Fig. 5a), the images were exhibited the elemental composition (C, O, Mg, and Fe atoms) of the prepared sample.

For $\text{CA-MgFe}_2\text{O}_4$ NPs (Fig. 5b), the models were Fe, Mg, O, and C. Figure 5b verified the formation of the composite in terms of its components (C, O, Mg, and Fe atoms). Interestingly, images of elemental mapping confirmed the creation of a surface coated system, revealed by brightness and darkness of its layers, MgFe_2O_4 NPs which were located at the core were relatively-darker than CA particles coated that core [72].

The relatively-brightest intensity of (C) atoms showed that CA particles is the external layer and has the highest ratio (red arrow), followed by another relatively less-bright particles attributed to MgFe_2O_4 NPs (yellow circles). Furthermore, both (Mg) and (Fe) atoms (the principal metals in ferrite) were distributed equally in the same place.

Positively, it is the first time to use elemental mapping as a tool to illustrate the development of a concentric structure which can give a promising explanation about the

distribution and purity of the atoms and layers forming the nanocomposites [18, 73, 74].

Shape and Size of the Synthesized $\text{CA-MgFe}_2\text{O}_4$ NPs and MgFe_2O_4 NPs Using HRTEM Analysis

The synthesized MgFe_2O_4 NPs appears as a semi-spherical shape and small sizes as shown in Fig. 6a. The detected sizes were varied from 12.15 to 49.21 nm and the average particle size was determined to be 23.01 nm.

On the other hand, $\text{CA-MgFe}_2\text{O}_4$ NPs generally have spherical shape with smooth surfaces with a narrow size distribution. Figure 6b shows the typical HRTEM images of calcinated $\text{CA-MgFe}_2\text{O}_4$ nanopowder. It can be seen from the HRTEM image that the particles are spherical in shape with uniform size distribution. The size of these particles is controllable to be from 14.25 nm to 58.15 nm with average 31.40 nm in diameter which larger than the synthesized MgFe_2O_4 NPs due to the loading of CA on the surface. Our results accepts with the size determined by Williamson–Hall (W–H) from X-ray diffraction studies.

Surface Charge Determination: Zeta Potential Analysis

The Zeta potential of the synthesized MgFe_2O_4 NPs and $\text{CA-MgFe}_2\text{O}_4$ NPs was examined at various pH such as 3, 7, and 9 as observed in Fig. 7. From the present results, it can be found that the Zeta potential of MgFe_2O_4 NPs and $\text{CA-MgFe}_2\text{O}_4$ NPs surface maintains a negative statement at pH 7 and 9, while owns a positive charge at pH 3.

At acidic medium (pH 3), the initial Zeta potential of MgFe_2O_4 NPs was 39.3 mV (Fig. 7a), which completely-agrees with the previous results obtained before [75]. After the functionalization of CA on MgFe_2O_4 NPs surface the

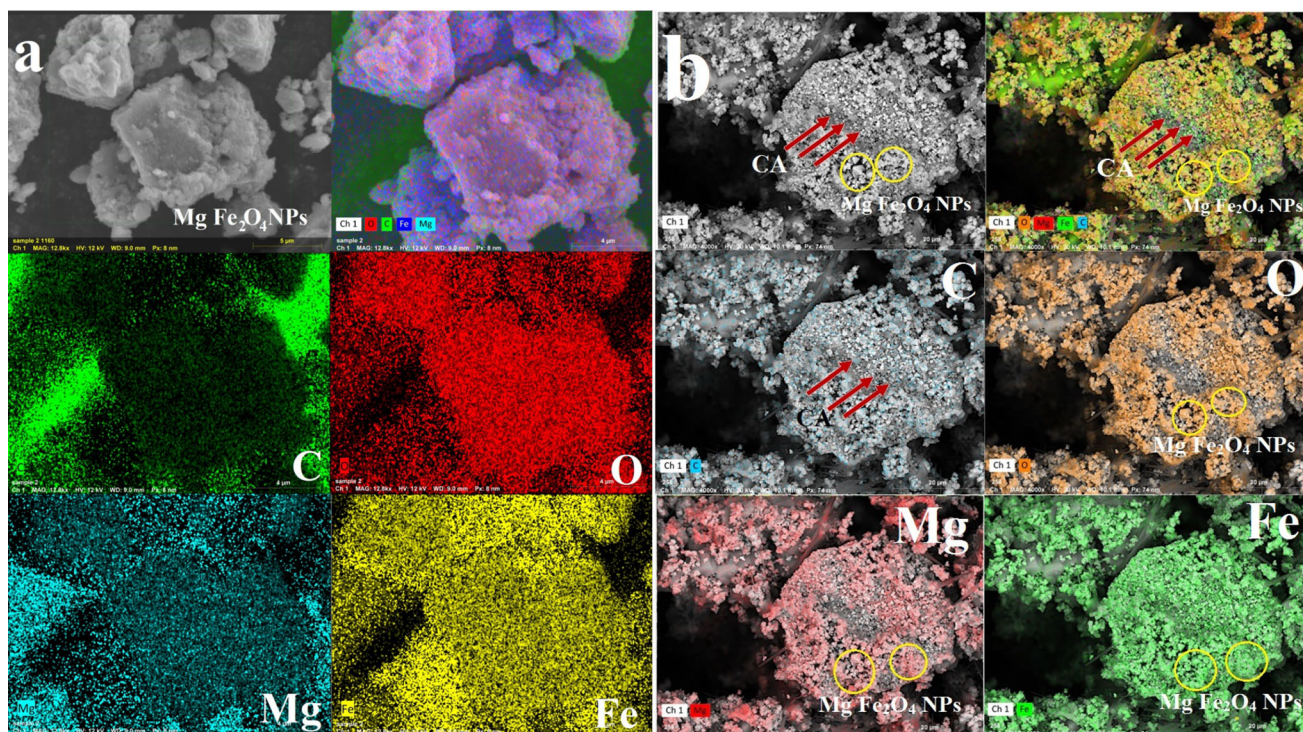


Fig. 5 Investigation of the purity and elemental distribution of **a** MgFe_2O_4 NPs, and **b** $\text{CA-MgFe}_2\text{O}_4$ NPs using SEM/EDX-assisted chemical mapping method

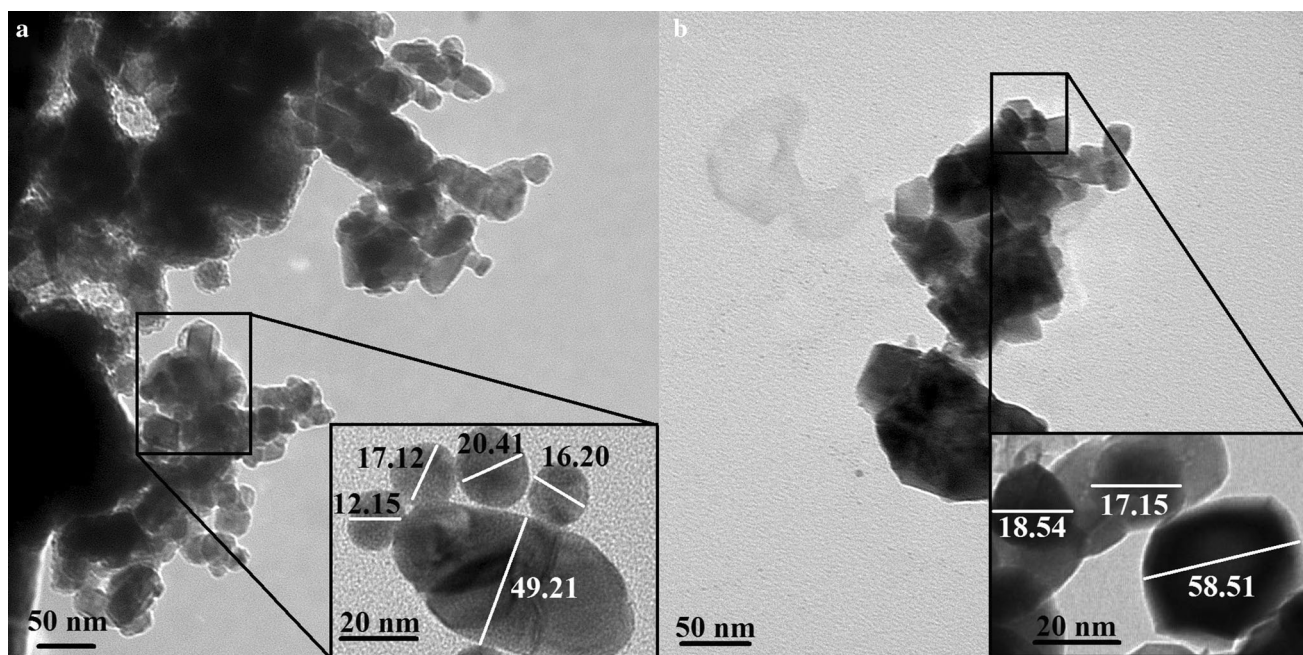


Fig. 6 Shape and size of the synthesized **a** MgFe_2O_4 NPs, and **b** $\text{CA-MgFe}_2\text{O}_4$ NPs using HRTEM analysis with high magnification (inserted)

potential was slightly-changed and decreased to be 36.5 mV due to the negative charge of CA and the net charge still positive as shown in Fig. 7b [76, 77]. Additionally, at neutral medium (pH 7), the Zeta potential of

MgFe_2O_4 NPs was -30.5 mV, (Fig. 7c), and after the functionalization of CA on MgFe_2O_4 NPs surface the potential was slightly-changed to be -36.9 mV due to the negative charge of CA as presented in Fig. 7d. Finally, at

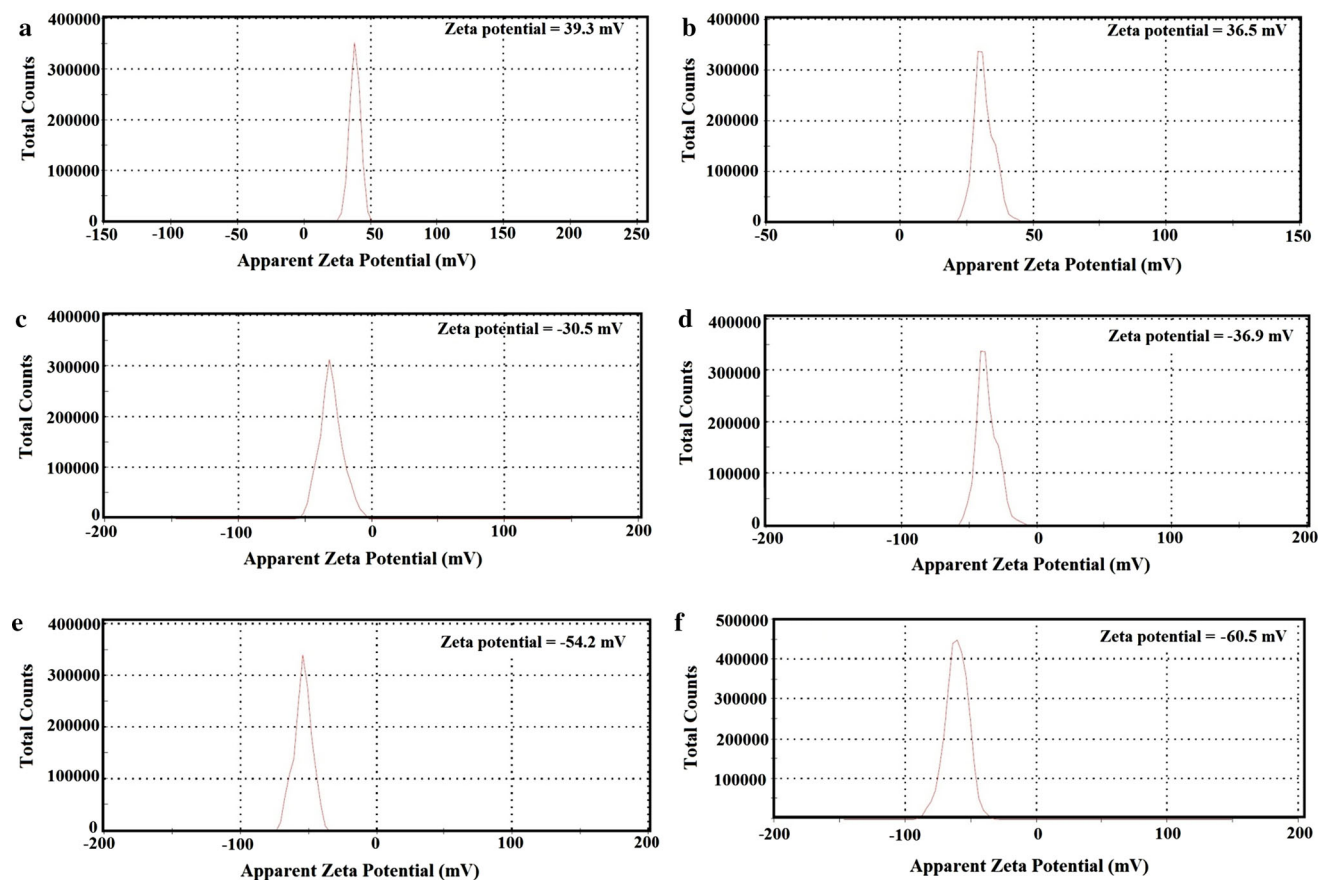


Fig. 7 Surface charge determination by zeta potential where (a, c, and e) for MgFe₂O₄ NPs at pH 3, 7, and 9, respectively, and (b, d, and f) for CA-MgFe₂O₄ NPs at pH 3, 7, and 9, respectively

alkaline medium (pH 9), the Zeta potential of MgFe₂O₄ NPs was -54.2 mV, (Fig. 7e), and after the functionalization of CA on MgFe₂O₄ NPs surface the potential was changed to be -60.5 mV due to the negative charge of CA as presented in Fig. 7f.

Removal Performance of CA-MgFe₂O₄ NPs toward Methyl Orange (MO)

The MO removal was monitored spectrophotometrically at the absorbance maximum of MO dye viz. $\lambda_{\max} = 464$ nm as shown in Fig. 8a. The calibration curve of MO was done using serial dilution (5, 10, 20 and 30 ppm) of MO as illustrated in Fig. 8b.

Effect of pH on Removal of MO

For removal studies, one of the vital factors is its dependence on pH of the solution. On investigating the pH dependence of the MO removal by CA functionalized MgFe₂O₄ NPs, that the MO removal efficiency increases obviously with increasing pH from 3 to 5 and achieves the maximum at pH 5, and then decreases as shown in Fig. 9a.

A plot showing the variation of MO removal (%) with time at different solution pH (3.0–9.0) was exhibited in Fig. 9b. The maximum MO removal (%) $\sim 75.5\%$ in equilibrium was observed at pH 5.0. Hence, all the further removal experiments were conducted at pH 5.0 in this study. Decrease in removal efficiency at the highest pH values may be due to the de-protonation of the CA-MgFe₂O₄ and competitive interaction between hydroxyl ions and anionic part of MO molecule present in the reaction solution as mentioned in [78].

To determine the point of zero charge (PZC) of the CA-MgFe₂O₄ nanocomposite, 0.1 g (CA-MgFe₂O₄ NPs) was added to 50 ml (0.01 M NaCl solution). The pH values of the solutions were adjusted with HCl or NaOH to be as 2, 4, 6, 8, 10, and 12. The samples were stirred at 200 rpm for 48 h.

The pH values of the solutions were measured after magnetically-separation of CA-MgFe₂O₄ nanocomposite. The pH of the PZC value was determined by using a plot which shows the final pH versus initial pH. These results was presented in Fig. 9. According to Fig. 9, the pH of the PZC occurred where there is no significant difference between final and initial pH values, and was determined to

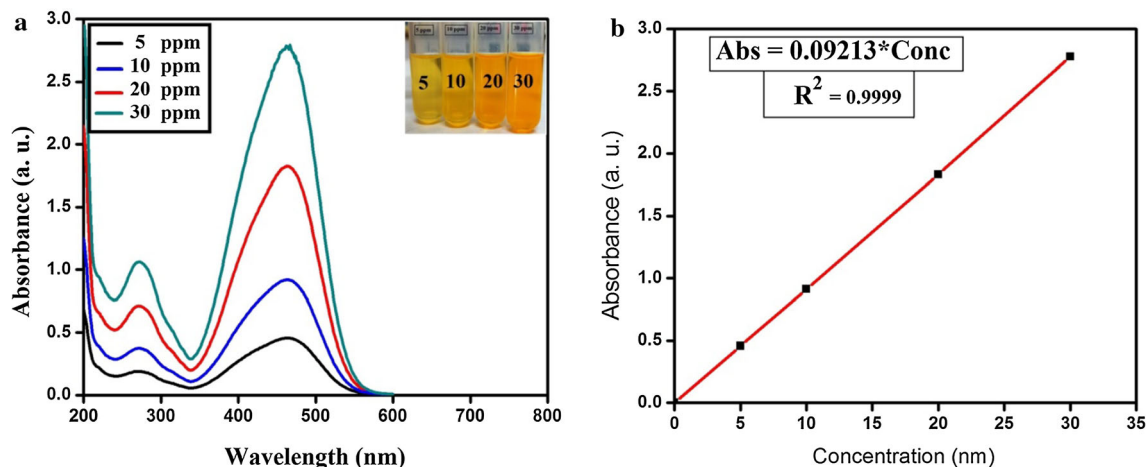


Fig. 8 a UV spectrum of MO at $\lambda_{max} = 464$ nm at different concentrations, and b the calibration curve of MO using (5, 10, 20, 30 ppm)

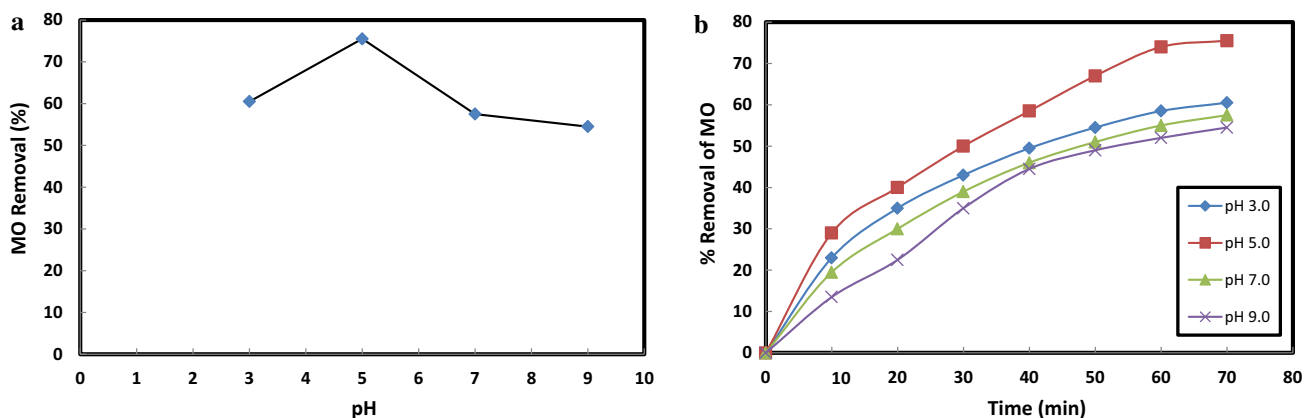


Fig. 9 a Effect of pH on MO removal efficiency, and b a plot showing the variation of MO removal (%) with time at different solution pH (3.0–9.0) (0.1 g of CA-MgFe₂O₄ in 50 ml of 20 mg/l MO at 25 °C)

be at pH 6.2. It means that the surface charge of the (CA-MgFe₂O₄) is positive and negative when $pH < pH$ of PZC and $pH > pH$ PZC, respectively. Besides, when the pH of the solution is equivalent to the pH of the PZC, the CA-MgFe₂O₄ nanocomposite surface charge is neutral [79].

According to the pH of the PZC value, the pH of the PZC regarding CA-MgFe₂O₄ nanocomposite was 6.2 and this result was explained why the removal of MO was maximum at pH 5.0 as displayed in Fig. 10. Hence at this point the net surface charge of the CA-MgFe₂O₄ nanocomposite is positive which attracted with the negative charge of MO and improve the removal of MO (the results were agreed with the zeta potential results; Fig. 7).

The removal of MO began to decrease at pH 7.0 this occur due to the repulsion forces between the negative charge of MO and net surface charge of the CA-MgFe₂O₄ nanocomposite which is negative at $pH < 6.2$. The reason which make the removal activity decreases at pH 5.0 unexpectedly is at highly acidic medium the metal oxide

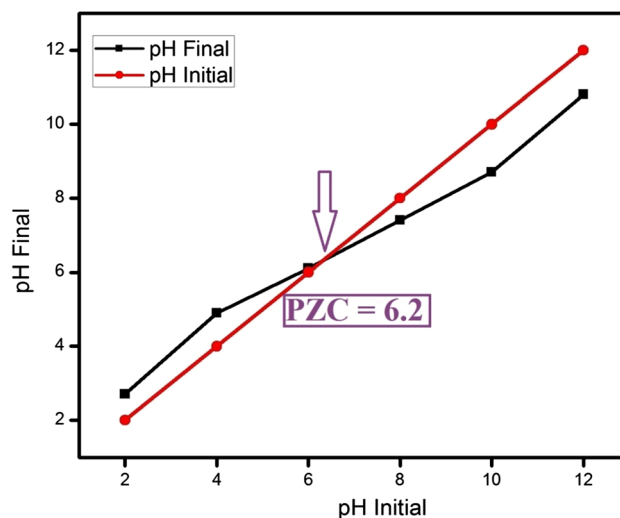


Fig. 10 Point of zero charge (PZC) of CA-MgFe₂O₄ at different pH

leaching may be occur which decrease the catalyst concentration [79].

Effect of Initial Concentration of MO

As the initial MO concentration plays a vital role in the removal process, the effect of ionic strength of MO was studied by varying the initial concentration of MO and keeping other reaction conditions unaltered. Figure 11a represents the variation of removal % as a function of contact time at different initial MO concentration (10, 20 and 30 mg/l).

At higher concentration of MO, the removal % was recorded to be high. The higher removal % at higher MO concentration is because of the stronger interaction with the CA-MgFe₂O₄ NPs at the higher ionic concentration of MO as noted in [80].

Effect of CA-MgFe₂O₄ NPs Dose

The effect of CA-MgFe₂O₄ NPs dose on the removal process was studied by keeping other parameters such as initial MO concentration, pH of the solution, and temperature fixed. Figure 11b depicts the effect of CA-MgFe₂O₄ NPs dose on MO removal process, where the dose amount of CA-MgFe₂O₄ NPs was varied (0.05–0.1 and 0.2) g.

During this study, the initial concentration of MO was kept constant at 20 mg/l and the pH of the system was kept at 5.0 at room temperature. It was observed that the percentage removal of MO depends on the CA-MgFe₂O₄ NPs dose significantly and increases with increasing dose. These can be attributed to the increase of the available active sites with the increase of adsorbent dose [81]. From the Fig. 11b, it is noticed that percentage removal of MO approaches nearing 85% at a dose of 0.1 g with the above-mentioned experimental condition.

Kinetic Studies

The degradation rates of MO can be represented by the following Eq. 3:

$$-\ln C_t/C_0 = -Kt \quad (3)$$

where C_t and C_0 are the remaining and the initial concentrations of methyl orange respectively, while t is the removal time and k represent the removal rate constant.

Figure 12a shows a relation of $-\ln C_t/C_0$ vs. t . The results shown that, the removal reaction kinetics followed first-order rate laws ($R^2 > 98$) at wholly-dose of CA-MgFe₂O₄ NPs.

Moreover, as revealed from Fig. 12b, an increasing of CA-MgFe₂O₄ NPs dose leads the apparent first order rate constants to be decreased, which is indicating a non-elementary nature of the removal reactions. This reliance of reaction rate constants on CA-MgFe₂O₄ NPs dose matched well with presented literature [82, 83].

After conducting a comparison with related studies in the literature, Akeem et al. [84] synthesized CoO–NiFe₂O₄ nanocatalyst and studding the enhanced performance and recyclability for efficient decolorization of azo dye via Fenton-like reactions. The result indicating that the decolorization efficiency significantly-reduced to 19.8% in the alkaline conditions, where $\cdot\text{OH}$, O_2^- and photo-generated hole (h^+) were responsible for the effective decolorization.

Another study performed by Akeem et al. [85], related to the high boron removal by functionalized magnesium ferrite nano-powders. Results were showed that polyvinyl alcohol-functionalized magnesium ferrites removed 93% of boron at 5 mg/L at pH 7 in 30 min., whereas only 68% of boron was removed by glycidol-functionalized magnesium ferrites. However, at higher boron concentration, of 50 mg/L, glycidol-functionalized magnesium ferrite showed higher adsorption affinity of 68.9 mg/g.

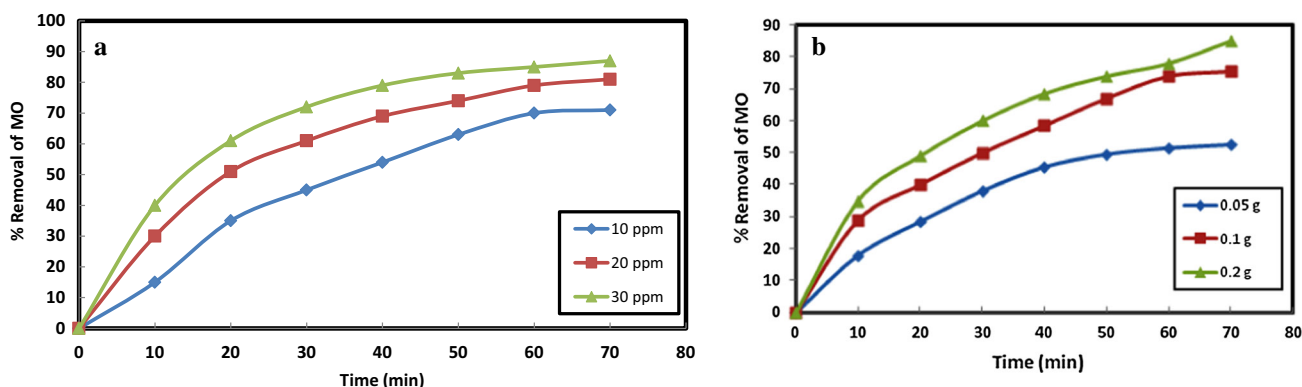


Fig. 11 **a** The variation of adsorption capacity as a function of contact time at different initial MO concentration (10, 20 and 30 mg/l) at pH 5.0 and 0.1 g CA-MgFe₂O₄, and **b** effect of adsorbent dose on MO removal at pH 5.0 and 10 mg/l MO

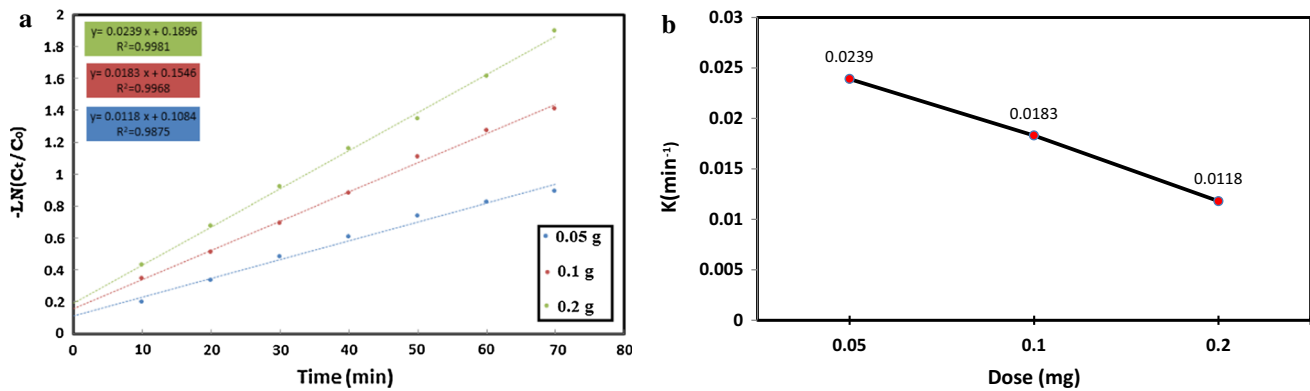


Fig. 12 **a** Kinetic studies as a relation of $-\ln C_t/C_0$ vs. t , and **b** shows a relation of CA-MgFe₂O₄ dose vs. Rate constant

In Vitro Antimicrobial Activity of the Synthesized CA-MgFe₂O₄ NPs, CA, and MgFe₂O₄ NPs

It is observed from the disc agar diffusion process (as a screening method) that the CA-MgFe₂O₄ NPs and MgFe₂O₄ NPs represented a qualitative antimicrobial potential against all the tested bacteria and *Candida* pathogens. The in vitro ZOI result confirmed that CA-MgFe₂O₄ NPs showed its approved antibacterial activity against *S. aureus* (20.0 mm ZOI; Fig. 13a), and *E. coli* (16.0 mm ZOI; Fig. 13b) as presented in Table 1.

It worth recognizing that, the antibacterial influence of CA-MgFe₂O₄ NPs was significantly-stronger than MgFe₂O₄ NPs, CA, and a standard antibacterial agent (Gentamycin; CN).

It is important to assume that; the incorporated CA-MgFe₂O₄ NPs were active against Gram-positive bacteria more than Gram-negative. The cell walls constituents in Gram-negative bacteria include basically-layers of lipopolysaccharide, lipid, and peptidoglycan, while the cell walls of Gram-positive combine very compact peptidoglycan forms [86]. Additionally, the synthesized CA-MgFe₂O₄ NPs were encouraged antifungal agents, and they showed great antifungal efficacy against *C. albicans* (14.0 mm ZOI; Fig. 13c) as shown in Table 1.

There is a link between the characteristics of CA-MgFe₂O₄ NPs and the antimicrobial results. The crystal size of CA-MgFe₂O₄ NPs was small (18.35 nm; Fig. 2b), and distributed as a spherical particle with particle size calculated at 31.40 nm (Fig. 6b), purity and pure elemental analysis (EDX; Fig. 4b) and highly-distributed NPs (Fig. 3b) which accepted as a primary goal in improving the antimicrobial strength of CA-MgFe₂O₄ NPs at low concentration (20.0 µg/ml), against all the examined bacteria and *Candida* sp.

The synthesized samples showed different physical and chemical features different than traditional organic and

artificial antimicrobial agents such as the decreased crystal size and average particle size, more stability, and higher strength for interaction with more pathogenic bacteria and *Candida* sp., therefore improving their antimicrobial potential [18, 87].

The MIC results of CA-MgFe₂O₄ NPs against all the tested pathogenic bacteria and *Candida* sp. were in the range from 10.0 to 1.250 µg/ml as mentioned in Table 1. CA-MgFe₂O₄ NPs possess promising MIC of 1.250 µg/ml against *S. aureus*. The size of CA-MgFe₂O₄ NPs was not only a parameter showing the antimicrobial characteristics, but other features such as mono-dispersity, stability, and shape should be considered [88]. Related reports [18, 36, 64, 69, 89–91] would be taught the performance of metal-ferrite NPs as antimicrobial agents against the pathogenic microbes as well listed in details in Table 2.

To explain the antimicrobial potential of CA-MgFe₂O₄ NPs, we tried to show the action mechanism against *E. coli* and *C. albicans* applying the SEM/EDX analysis (Fig. 14) [92, 93]. SEM images were showed the shape of bacterial and yeast cells before and after CA-MgFe₂O₄ NPs treatment. In the control sample (non-treated bacterial and yeast cells), bacterial and yeast colonies were regularly-grown and displayed normal cellular shapes with the typical cell surface and combined biofilm, as shown in Fig. 14a, b.

After the treatment with CA-MgFe₂O₄ NPs, noticeable morphological variations were identified in *E. coli* and *C. albicans* cells (Fig. 14c, d). Also, visible lysis of the outer surface was accompanied by deformations and reductions in the viable number of *E. coli* and *C. albicans* cells. Furthermore, biofilm development was inhibited. EDX elemental analysis exposed the presence of Mg, O, and Fe atoms and C atoms for CA at the deformed areas and the outer surface of the treated *E. coli* and *C. albicans* cells, affirming the action of the tested CA-MgFe₂O₄ NPs, as shown in Fig. 14e, f.

One probable reason for the highest activity against the cells of *E. coli* and *C. albicans* could be the large surface

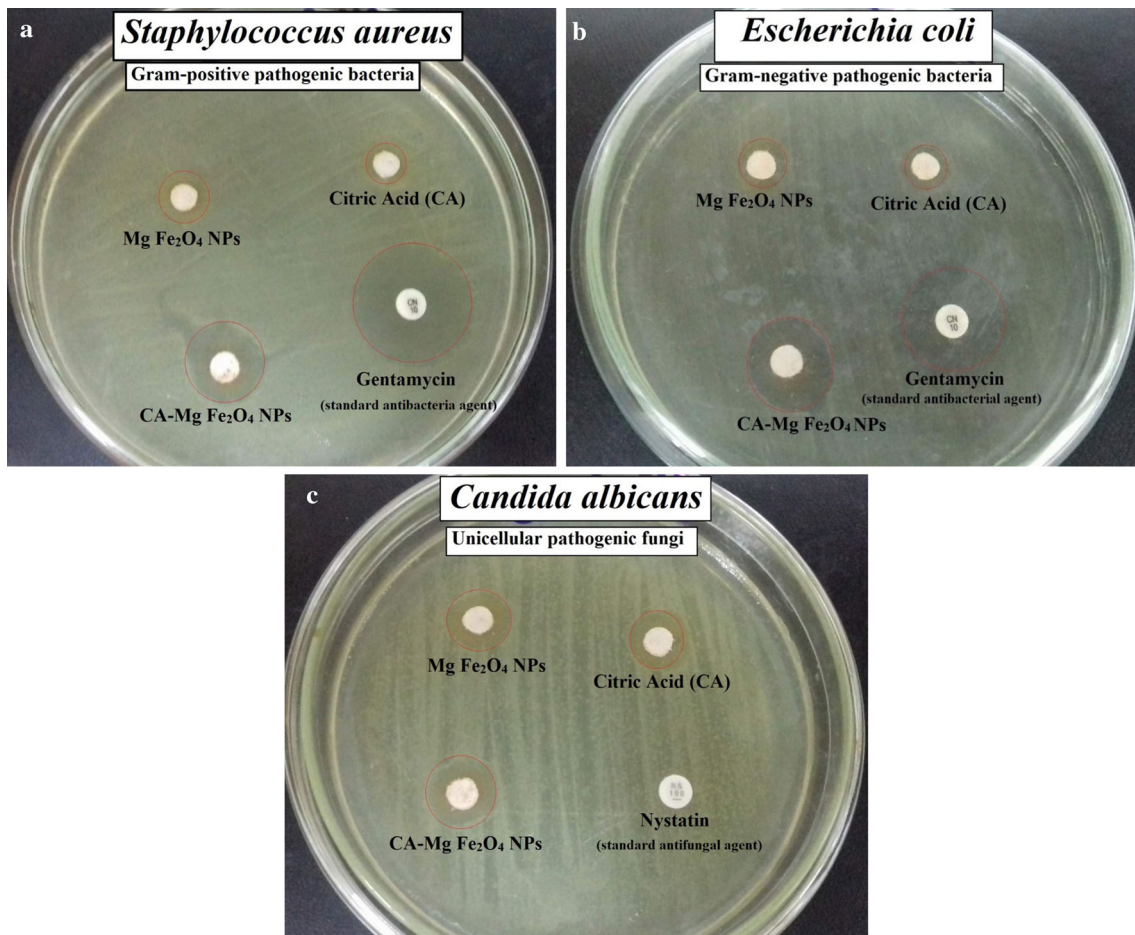


Fig. 13 Antimicrobial activity of CA-Mg Fe₂O₄ NPs, Mg Fe₂O₄ NPs and citric acid (CA) against multi-drug resistant (MDR) bacteria, and pathogenic *Candida* species measured as ZOI (mm): where **a** *Staphylococcus aureus*, **b** *Escherichia coli*, and **c** *Candida albicans*

Table 1 Antibacterial and antifungal activities of CA-MgFe₂O₄ NPs, MgFe₂O₄ NPs and Citric Acid (CA) against multi-drug resistant (MDR) bacteria, and pathogenic *Candida* species measured as ZOI (mm) and MIC (μg/ml)

Pathogenic microbes	ZOI of CA-MgFe ₂ O ₄ NPs (20.0 μg/ml) (mm)	MIC of CA-MgFe ₂ O ₄ NPs (beginning with 20.0 μg/ml) (μg/ml)	ZOI of MgFe ₂ O ₄ NPs (20.0 μg/ml) (mm)	MIC of MgFe ₂ O ₄ NPs (beginning with 20.0 μg/ml) (μg/ml)	ZOI of CA (mm)	CN or NS
<i>Escherichia coli</i>	16.0 ^c ± 0.5000	2.5	11.0 ^b ± 0.2645	10.0	9.0 ^a ± 0.2516	15.0 ^b ± 0.3055
<i>Pseudomonas aeruginosa</i>	13.0 ^a ± 0.2645	5.0	9.0 ^a ± 0.4041	10.0	Nil	Nil
<i>Staphylococcus aureus</i>	20.0 ^d ± 0.4932	1.25	12.0 ^c ± 0.4000	10.0	11.0 ^b ± 0.2081	26.0 ^c ± 0.5291
<i>Bacillus subtilis</i>	13.0 ^a ± 0.2645	5.0	12.0 ^c ± 0.4358	10.0	Nil	7.0 ^a ± 0.3214
<i>Candida albicans</i>	14.0 ^b ± 0.4041	2.5	12.0 ^c ± 0.3785	5.0	11.0 ^b ± 0.2645	Nil
LSD	1.13333	–	0.90000	–	2.20000	7.90000

Values are presented as mean ± SD (n = 3). Data within the groups were analyzed using one-way analysis of variance (ANOVA) followed by a,b,c,d,e Duncan's multiple range test (DMRT)

Nil means that, no ZOI has been measured

LSD least significant difference, CN Gentamycin; 20 μg/ml (standard antibacterial agent), NS Nystatin (standard antifungal agent)

Table 2 Comparative antimicrobial studies between different synthesized ferrites in the biomedical field

Methods of ferrites synthesis	Average crystal size (nm)	Starting concentration ($\mu\text{g/ml}$)	Antimicrobial activity (ZOI; mm) and/or (MIC; $\mu\text{g/ml}$)	References
Co-precipitation method	18.35	20 $\mu\text{g/ml}$ for ZOI and MIC	20 mm ZOI and 1.25 $\mu\text{g/ml}$ MIC	Our research
Facile sol–gel method	13–38.3	20 $\mu\text{g/ml}$ for ZOI and 100 $\mu\text{g/ml}$ for MIC	25 mm ZOI and 0.04 $\mu\text{g/ml}$ MIC	[36]
Sol–gel process	14–20	1 mg/ml for ZOI	15 mm ZOI	[89]
Self-combustion and wet ferritization methods	18.8	10 $\mu\text{g/ml}$ for ZOI	10 mm ZOI and 0.125 $\mu\text{g/ml}$ MIC	[90]
Microwave-assists biogenic synthesis using plant extract	24–32	100 $\mu\text{g/ml}$ for ZOI	25 mm ZOI	[91]
Sol–gel technique	13.04–30.96	5000 $\mu\text{g/ml}$ for ZOI	16 mm ZOI	[64]
Sol–gel technique utilizing citric acid and ethylene glycol as a polymerization agent	12.86–33.92	1000 $\mu\text{g/ml}$ for ZOI	28 mm ZOI	[69]
Citrate sol–gel method.	11.73–33.50	20 $\mu\text{g/ml}$ for ZOI	15 mm ZOI	[18]

area, small size, and purity of the synthesized CA-MgFe₂O₄ NPs which provides for a fixed impassive connection between the bacterial cell walls and the CA-MgFe₂O₄ NPs, as shown in Fig. 14c, d [50, 94]. This result is in a good agreement with various published reports on the interaction between metal oxide NPs and pathogenic microorganisms by electrostatic potential, resulting in bacterial membrane damage [50, 95, 96].

A recent study reported that metal oxide NPs could induce oxidative stress in pathogenic microbes [97], and quickly-damage their cell membranes after the exposure to increased cellular ROS levels. In this study, the prepared CA-MgFe₂O₄ NPs were attached to *E. coli* and *C. albicans* cells through electrostatic attraction and reduced microbial cell numbers via membrane leakages [95]. Our proposed action mechanism began with the adhesion of the CA-MgFe₂O₄ NPs to the outer surface of *E. coli* and *C. albicans*. Then, Fe²⁺ and Mg²⁺ ions penetrated the bacterial and yeast cells and damaged their biological molecules, such as mitochondria and DNA. After that, the cellular toxicity had been noted due to the oxidative stress and the created ROS.

On the other hand, the antimicrobial mechanism of the synthesized ferrite NPs is not recognized yet. There were remarkably-suggested mechanisms such as Reactive Oxygen Species (ROS) production ($\bullet\text{O}_2^-$ and $\bullet\text{OH}$) which depends on the crystallite size and surface area [98].

ROS creation occurs after the prepared ferrite NPs get contacts within the bacterial cell in the presence of light, which begins the excitation of the electrons from the valence band to the covalent band with a new energy level that exit h^+ in the valence band [99]. The produced ROS creating serious injury result when interact with the

biological macromolecules inside the bacterial cell such as DNA, lipids, proteins, and carbohydrates [100].

El-Batal et al. [101], have declared that four mechanisms interpret the action of metal NPs on the microbial pathogens. They found that Mg and Fe metals in ferrites nano-structure were started by the adhesion across the surface of the bacterial cell wall. After that, they were represented nano-metals (Mg and Fe) inside the bacterial cell and break all of the intracellular organization like biological molecules. Then, the cellular toxicity (oxidative stress) created by the formation of ROS was appeared. Finally, nano-metals (Mg and Fe) were affected the signal transduction pathways. Furthermore, the antibacterial potential of ferrite nano-structure may be due to the interaction with a specific enzyme that catalyzes mannose-6-phosphate exchange to fructose-6-phosphate by altering its configuration and subsequent its activity. Fructose-6-phosphate is an essential compound in the glycolysis pathway which is connected to the carbohydrate catabolism in all microbes [35].

There are many reports on antimicrobial activity of citric acid (CA) against *E. coli* [102, 103]. The *E. coli* were reduced by 1.52 logs when treated with CA for 10 min. Also, CA reduced microbial levels to greater extents than propionic acid and acetic acid in both apples and lettuce [104]. Treatment with 1.0% citric acid significantly-reduced the number of *E. coli* (3.0 log₁₀ CFU/g) after 5 min in ice berg lettuce [105].

After conducting a comparison with related studies in the literature, Zirar et al. [106], synthesized chitosan/metal oxide nanocomposites and studding the antibacterial activity. The result indicating that all the samples exhibited antibacterial activities against *E. coli* and *S. aureus*;

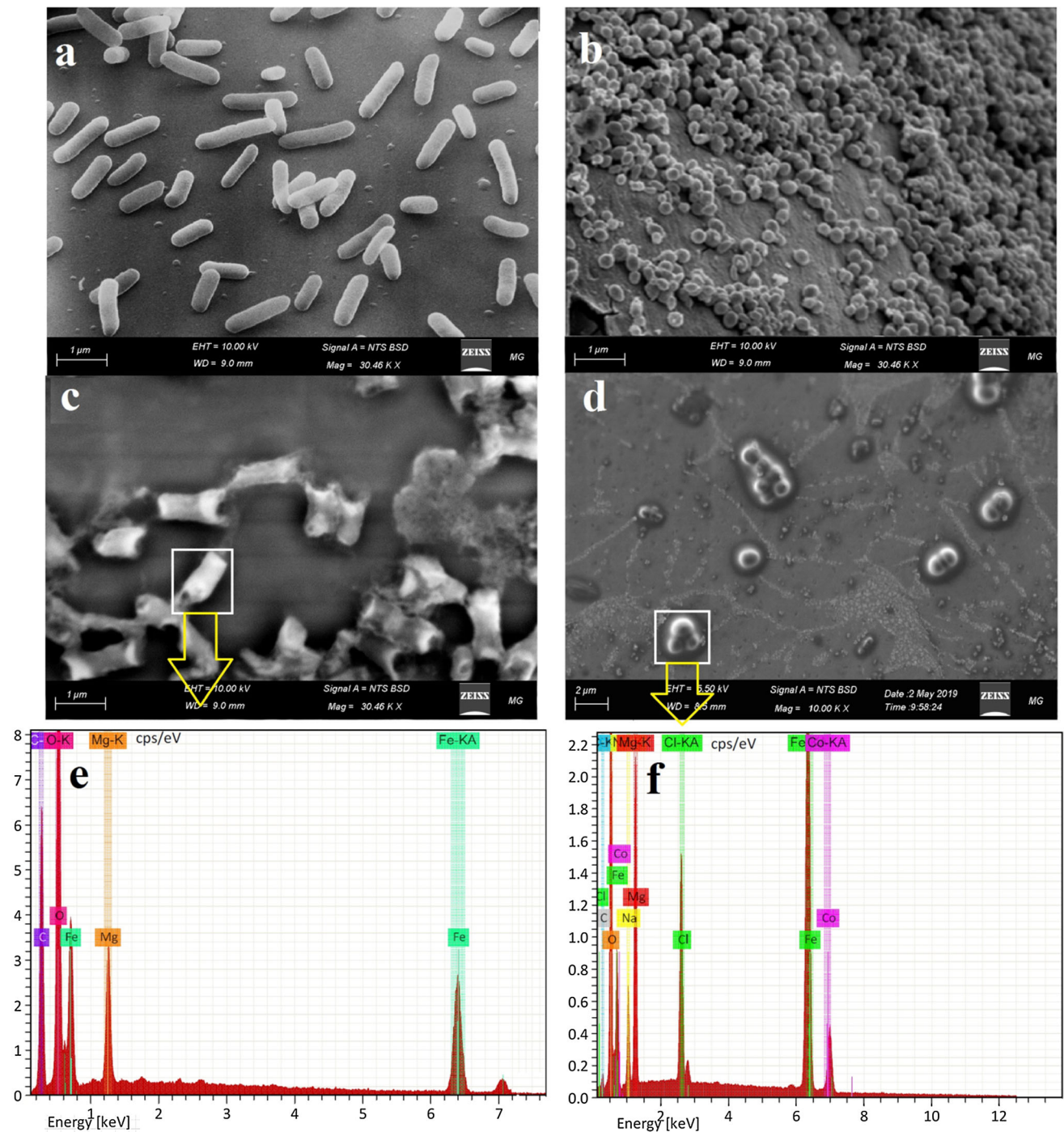


Fig. 14 SEM and corresponding EDX elemental analysis of *E. coli* and *C. albicans*: **a** Normal bacterial cells (*E. coli*) without CA-Mg Fe_2O_4 NPs treatment, **b** Normal yeast cells (*C. albicans*) without CA-Mg Fe_2O_4 NPs treatment, **c** depressed and deformed bacterial cell after CA-Mg Fe_2O_4 NPs treatment, **d** Depressed and deformed *Candida* cell by CA-Mg Fe_2O_4 NPs treatment showing the complete

lysis of *Candida* cell and loss of budding formation, **e** Corresponding EDX elemental analysis of the treated *E. coli* cell confirming the cellular internalization of the prepared CA-Mg Fe_2O_4 NPs in *E. coli* cells, and **f** Corresponding EDX elemental analysis of the treated *C. albicans* cell confirming the cellular internalization of the synthesized CA-Mg Fe_2O_4 NPs in *C. albicans* cells

however, more effective against *S. aureus* compared to *E. coli*. Noticeably, 5 $\mu\text{g}/\text{ml}$ chitosan-nickel oxide comparatively-exhibited the highest bactericidal capability where *E. coli* and *S. aureus* viabilities were reduced to

25–47% after 12 h incubation. After treatment with 15 $\mu\text{g}/\text{ml}$ of chitosan-nickel oxide, about 98% of *S. aureus* and 92.3% of *E. coli* cells were inhibited.

Conclusion

Based on XRD, HRTEM, and SEM analyses, it was founded that MgFe₂O₄ NPs were located at the core, while the CA was coated this core, producing CA-functionalized MgFe₂O₄ NPs with particle size about 31.40 nm in diameter. The surface behavior reveals inhomogeneous grain appearance with remarkable smooth agglomerates can be observed due to the occupation of a large quantity of Mg at the grain boundary which could control the grain growth. From FT-IR results, the two intense peaks observed between 580 and 484 cm⁻¹ were attributed to the stretching vibration mode associated with the metal–oxygen (Fe–O) bond in the crystalline lattice of Fe₂O₄. The in vitro ZOI and MIC results verified that CA-MgFe₂O₄ NPs exhibited its encouraged antimicrobial activity against *S. aureus* (20.0 mm ZOI & 1.25 µg/ml MIC), *E. coli* (16.0 mm ZOI & 2.5 µg/ml MIC), and *C. albicans* (14.0 mm ZOI & 2.5 µg/ml MIC). So, there is no toxicity regarding the use of CA-MgFe₂O₄ NPs in different fields. It should be noted that CA-MgFe₂O₄ NPs are also active upon Gram-positive than Gram-negative bacteria. In the control sample, bacterial and yeast colonies were regularly-grown and exhibited normal cellular shapes with the ideal cell surface and concentrated biofilm. While, after CA-MgFe₂O₄ NPs treatment, observable morphological changes were recognized in *E. coli* and *C. albicans* cells, and observable lysis of the external surface was accompanied by deformations and reductions in the viable number of *E. coli* and *C. albicans* cells. Results obtained from the removal activity indicated that citric acid-coated MgFe₂O₄ NPs (1.0 g/l) was a promising removal agent achieving 85.0% removal of MO in the slightly-acidic solution (pH 5.0). The synthesized CA-MgFe₂O₄ NPs are promising for potential applications in industry, food processing and packaging, pharmaceutical uses, wastewater treatment, and cosmetics.

Funding Not applicable.

Compliance with Ethical Standards

Conflict of interest The authors declare that they have no conflict of interest.

Research involving Human Participation and/or Animals Not applicable.

Informed Consent Not applicable.

Ethical Approval Not applicable.

References

1. E. Hill and R. DiSalvo (2019). *Environ. Epidemiol.* **3**, 159.
2. T. Hao, et al. (2014). *Appl. Surf. Sci.* **292**, 174–180.
3. X. Qin, et al. (2009). *J. Hazard. Mater.* **172**, (2–3), 1168–1174.
4. A. Debnath, et al. (2016). *Desal. Water Treat.* **57**, (29), 13549–13560.
5. Y. S. Reddy, et al. (2018). *J. Phys. Chem. Solids* **123**, 43–51.
6. R. Javaid and U. Y. Qazi (2019). *Intl. J. Environ. Res. Public Health* **16**, (11), 2066.
7. S. Mani, P. Chowdhary, and R. N. Bharagava Textile wastewater dyes: toxicity profile and treatment approaches. *Emerging and Eco-Friendly Approaches for Waste Management* (Springer, Berlin, 2019), pp. 219–244.
8. P. Zhang, et al. (2014). *J. Colloid Interface Sci.* **426**, 44–47.
9. T. V. Kumar, et al. (2018). *Appl. Surf. Sci.* **449**, 719–728.
10. K.-W. Jung, et al. (2018). *J. Ind. Eng. Chem.* **59**, 149–159.
11. M. N. Zafar, et al. (2018). *J. Clean. Prod.* **199**, 983–994.
12. D. Yimin, et al. (2018). *Colloids Surf. A* **550**, 90–98.
13. N. Deihimi, M. Irannajad, and B. Rezai (2018). *J. Environ. Manage.* **206**, 266–275.
14. B. Aşçi, B., et al. (2018). *Kinetic, isotherm and thermodynamic investigations of nitrite (NO₂⁻) removal from water by anion exchange resins.*
15. A. Jouali, et al. (2019). *J. Photochem. Photobiol. A* **383**, 112013.
16. F. Echabbi, et al. (2019). *J. Environ. Chem. Eng.* **7**, (5), 103293.
17. A. I. El-Batal, et al. (2017). *J. Photochem. Photobiol. B* **173**, 120–139.
18. M. I. A. A. Maksoud, et al. (2019). *Microb. Pathog.* **127**, 144–158.
19. V. Katheresan, J. Kannedo, and S. Y. Lau (2018). *J. Environ. Chem. Eng.*
20. D. Zaman, M. K. Tiwari, and S. Mishra *Measurement, Analysis and Remediation of Environmental Pollutants* (Springer, Singapore, 2019), p. 397.
21. A. Mittal and V. K. Gupta (2010). *Toxicol. Environ. Chem.* **92**, (10), 1813–1823.
22. J. Carvalho, J. Araujo, and F. Castro (2011). *Waste Biomass Valor.* **2**, (2), 157–167.
23. J. Mittal, et al. (2014). *Desal. Water Treat.* **52**, (22–24), 4508–4519.
24. A. Anjum Adsorption Technology for Removal of Toxic Pollutants. *Sustainable Heavy Metal Remediation* (Springer, Berlin, 2017), pp. 25–80.
25. K. T. Rainerta, et al. (2017). *Desal. Water Treat.* **86**, 203–212.
26. S. Bhattacharya, et al. (2013). *Int. J. Chem. Sci. Technol.* **3**, (3), 59–64.
27. G. L. Hornyak, et al. *Introduction to Nanoscience and Nanotechnology* (CRC Press, Boca Raton, 2008).
28. P. A. Cox *Transition Metal Oxides: An Introduction to Their Electronic Structure and Properties* (Oxford University Press, Oxford, 2010).
29. X. Qu, P. J. Alvarez, and Q. Li (2013). *Water Res.* **47**, (12), 3931–3946.
30. X. Chen, et al. (2018). *Adv. Mater.* **30**, (3), 1703950.
31. G. Govindasamy, et al. (2019). *J. Mater. Sci.: Mater. Electron.* **30**, (17), 16463–16477.
32. C. W. Wong, et al. (2019). *J. Clust. Sci.*
33. M. Abd Elkodous, et al. (2019). *Biological Trace Element Research.*
34. J. Jeevanandam, et al. in G. Szekely and A. Livingston (eds.), *Sustainable Nanoscale Engineering* (Elsevier, 2020), pp. 83–113.
35. M. A. Elkodous, et al. (2019). *J. Cluster Sci.* **30**, (3), 531–540.
36. M. I. A. Abdel Maksoud, et al. (2020). *J. Mater. Sci.*

37. G. S. El-Sayyad, F. M. Mosallam, and A. I. El-Batal (2018). *Adv. Powder Technol.* **29**, (11), 2616–2625.
38. A. El-Batal, et al. (2014). *Br. J. Pharm. Res.* **4**, (11), 1341.
39. E. E. Mbu (2018). *Photocatalytic degradation of azo and rhodamine dyes using nanostructured copper (II) oxide*. University of Ghana.
40. F. R. Zaggout, et al. (2005). *Mater. Lett.* **59**, (23), 2928–2931.
41. I. Gul, et al. (2007). *J. Magn. Magn. Mater.* **311**, (2), 494–499.
42. S. Mirzaee, Y. Azizian-Kalandaragh, and P. Rahimzadeh (2020). *Solid State Sci.* **99**, 106052.
43. A.-F. Lehlooh, et al. (2020). *Hyperfine Interact.* **241**, (1), 21.
44. M. Lattuada and T. A. Hatton (2007). *Langmuir* **23**, (4), 2158–2168.
45. P. Belavi, et al. (2012). *Mater. Chem. Phys.* **132**, (1), 138–144.
46. D. Winistörfer (1995). *Commun. Soil Sci. Plant Anal.* **26**, (7–8), 1073–1093.
47. A. I. El-Batal, et al. (2017). *J. Clust. Sci.* **28**, (3), 1083–1112.
48. A. Baraka, et al. (2017). *Chem. Pap.* **71**, (11), 2271–2281.
49. A. I. El-Batal, et al. (2018). *Microb. Pathog.* **118**, 159–169.
50. A. I. El-Batal, et al. (2018). *Int. J. Biol. Macromol.* **107**, 2298–2311.
51. A. S. Awed, et al. (2019). *J. Clust. Sci.*
52. M. Balouiri, M. Sadiki, and S. K. Ibsouda (2016). *J. Pharm. Anal.* **6**, (2), 71–79.
53. A. I. El-Batal, et al. (2019). *J. Clust. Sci.*
54. A. I. El-Batal, et al. (2019). *J. Cluster Sci.* **30**, (4), 947–964.
55. F. M. Mosallam, et al. (2018). *Microbial Pathogen.*
56. M. S. Attia, et al. (2019). *J. Clust. Sci.*
57. M. Abd Elkodous, et al. (2019). *Colloids Surf. B* **180**, 411–428.
58. M. A. Ansari, et al. (2014). *Appl. Nanosci.* **4**, (7), 859–868.
59. K. Brownlee (1952). *Probit Analysis: A Statistical Treatment of the Sigmoid Response Curve*. JSTOR.
60. B. D. Cardoso, et al. (2018). *R. Soc. Open Sci.* **5**, (10), 181017.
61. Q. Chen, et al. (1999). *J. Magn. Magn. Mater.* **194**, (1–3), 1–7.
62. M. Sheykhani, et al. (2012). *Tetrahedron Lett.* **53**, (24), 2959–2964.
63. S. T. Fardood, Z. Golfar, and A. Ramazani (2017). *J. Mater. Sci.* **28**, (22), 17002–17008.
64. A. H. Ashour, et al. (2018). *Particuology* **40**, 141–151.
65. T. K. Mahto, et al. (2015). *J. Nanosci. Nanotechnol.* **15**, (1), 273–280.
66. Z. Lin, et al. (2014). *J. Alloy Compd.* **588**, 30–35.
67. A. Sinha, T. Mahata, and B. Sharma (2002). *J. Nucl. Mater.* **301**, (2–3), 165–169.
68. R. O. Toro (2015). *Development and Characterization of Corn Starch Film by Blending with More Hydrophobic Compounds*. 2015, Doctoral Thesis, Universitat Politècnica De Valencia.
69. M. I. A. AbdelMaksoud, et al. (2018). *Mater. Sci. Eng. C* **92**, 644–656.
70. K. Zipare, S. Bandgar, and G. Shahane (2018). *J. Rare Earths* **36**, (1), 86–94.
71. K. M. Srinivasamurthy, et al. (2018). *Ceram. Int.* **44**, (8), 9194–9203.
72. P. Dobrowolska, et al. (2015). *Materials* **8**, (6), 2849–2862.
73. M. A. Maksoud, et al. (2019). *J. Mater. Sci.*
74. A. I. El-Batal, et al. (2019). *J. Clust. Sci.* **30**, (3), 687–705.
75. C. Aoopngan, et al. (2019). *ACS Appl. Nano Mater.* **2**, (8), 5329–5341.
76. F. Zhang, et al. (2019). *Ceram. Int.* **45**, (5), 5996–6003.
77. J. Nonkumwong, S. Ananta, and L. Srisombat (2016). *RSC Adv.* **6**, (53), 47382–47393.
78. L. Zhang, et al. (2015). *RSC Adv.* **5**, (114), 93840–93849.
79. M. Kumar and R. Tamilarasan (2013). *Pol. J. Chem. Technol.* **15**, (2), 29–39.
80. S. Khurshid, et al. (2020). *RSC Adv.* **10**, (2), 1021–1041.
81. M. R. Rezaii Mofrad, et al. (2016). *Desalin. Water Treat.* **57**, (18), 8330–8335.
82. D. L. Currell, G. Wilhelm, and S. Nagy (1963). *J. Am. Chem. Soc.* **85**, (2), 127–130.
83. A. K. Mathur, et al. (2008). *J. Hazard. Mater.* **157**, (2–3), 335–343.
84. A. A. Oladipo, A. O. Ifebajo, and M. Gazi (2019). *Appl. Catal. B* **243**, 243–252.
85. A. A. Oladipo and M. Gazi (2016). *Environ. Chem. Lett.* **14**, (3), 373–379.
86. Z.-X. Tang and B.-F. Lv (2014). *Braz. J. Chem. Eng.* **31**, (3), 591–601.
87. A. Ashour et al. (2018) *Particuology*.
88. S. Pal, Y. K. Tak, and J. M. Song (2007). *Appl. Environ. Microbiol.* **73**, (6), 1712–1720.
89. S. Xavier, et al. (2014). *Res. J. Pharm. Biol. Chem. Sci.* **5**, (5), 364–371.
90. D. Gingasu, et al. (2016). *J. Nanomater.*
91. M. M. Naik, et al. (2019) *J. Sol-Gel Sci. Technol.*, 1–18.
92. S. Priyadarshini, et al. (2019). *Res. Chem. Intermed.* 1–13.
93. A. I. El-Batal, et al. (2019). *J. Clust. Sci.*
94. A. El-Batal, et al. (2013). *J. Chem. Pharm. Res.* **5**, (8), 1–15.
95. P. K. Stoimenov, et al. (2002). *Langmuir* **18**, (17), 6679–6686.
96. A. I. El-Batal, F. M. Mosallam, and G. S. El-Sayyad, *J. Clust. Sci.* pp 1–13.
97. M. F. Khan, et al. (2016). *Sci. Rep.* **6**, 27689.
98. S. Ma, et al. (2019). *ACS Earth Space Chem.* **3**, (5), 738–747.
99. A. Hezma, A. Rajeh, and M. A. Mannaa (2019). *Colloids Surf., A* **581**, 123821.
100. G. S. El-Sayyad et al. (2019). *Biol. Trace Elem. Res.* 1–20.
101. A. I. El-Batal, F. M. Mosallam, and G. S. El-Sayyad (2018). *J. Clust. Sci.* **29**, (6), 1003–1015.
102. Y. W. In, et al. (2013). *J. Food Saf.* **33**, (1), 79–85.
103. S. Eswaranandam, N. Hettiarachchy, and M. Johnson (2004). *J. Food Sci.* **69**(3): FMS79-FMS84.
104. S. H. Park, et al. (2011). *J. Food Sci.* **76**, (6), M293–M298.
105. M. Akbas and H. Ölmez (2007). *Lett. Appl. Microbiol.* **44**, (6), 619–624.
106. Z. M. Mizwari, A. A. Oladipo, and E. Yilmaz (2020). *Int. J. Polym. Mater. Polym. Biomater.* pp. 1–9.

Publisher's Note Springer Nature remains neutral with regard to jurisdictional claims in published maps and institutional affiliations.